Green Chemistry

PAPER

View Article Online
View Journal | View Issue

Cite this: *Green Chem.*, 2025, **27**, 3905

Hydrocracking of polyolefins over ceria-promoted Ni/BEA catalysts†

Jessie A. Sun, [a,b] Esun Selvam,[a,b] Alexander Bregvadze,[a] Weiqing Zheng [a] and Dionisios G. Vlachos *[a,b,c]

Received 20th January 2025,
Accepted 14th March 2025

DOI: 10.1039/d5gc00345h

rsc.li/greenchem

Hydroconversion of polyolefins into primary petrochemical feedstocks, such as naphtha (C_5–C_{12}), offers a promising strategy to redirect plastic waste from landfills into the economy. Current hydrocracking strategies predominantly utilize precious metal-based catalysts, as the higher activation energy and stability issues limit the use of Earth-abundant metals (EAM). Herein, we improve the stability of Ni/BEA by incorporating a ceria promoter and demonstrate it in the hydrocracking of low-density polyethylene (LDPE). The Ce-promoted Ni/BEA catalyst achieved over 80% selectivity toward naphtha with the highest-reported naphtha productivity, outperforming current noble metal (Pt and Ru) and EAM (Ni and Co) catalysts. Catalyst evaluation and characterization underscore that ceria directly regulates metal dispersion and redox behavior and mitigates catalyst deactivation by suppressing coke formation. We correlate the promotional role of ceria to its unique hydrogen storage ability, which directly enhances metal hydrogenation ability. This work highlights exciting progress toward optimizing EAM hydrocracking catalysts for polyolefin upcycling.

Green foundation

1. The development of polyolefin (PO) deconstruction and upcycling chemistries helps divert plastic waste from landfills, enabling the conservation of the natural environment and non-renewable petrochemical resources. Optimization of Earth-abundant metal (EAM)-based catalysts is crucial for the industrial advancement of sustainable materials and PO waste deconstruction processes, thereby promoting the principles of green chemistry and furthering the field.
2. This work presents the use of a ceria-promoted Ni/BEA catalyst for low-density polyethylene (LDPE) hydrocracking. Notably, ceria-promoted Ni/BEA demonstrates high productivity for naphtha generation and the addition of ceria was shown to improve Ni reducibility, resistance to coking, and overall stability.
3. The ceria-promoted Ni/BEA catalyst exhibited enhanced hydrogenation ability even under hydrogen-lean conditions, revealing exciting opportunities for future tuning of reaction pressure requirements for increased energy efficiency.

Introduction

Plastics have become an irreplaceable commodity in modern society. However, their rapid consumption has led to the mismanagement of over 7000 Mt of end-of-life plastic waste, as only ~10% is recycled.[1–3] This has resulted in their accumulation in landfills, posing significant environmental and human health concerns. Polyolefins (POs) are the most prevalent polymers used today. Due to their structural simplicity and durability, they are widely employed across various societal sectors, including construction, transportation, and telecommunications.[4–6] Common POs, including high- and low-density polyethylene (HDPE and LDPE) and polypropylene (PP), constitute nearly 60% of the plastic waste generated annually and are prime candidates for chemical recycling *via* catalytic hydrocracking.[7] Hydrocracking utilizes a bifunctional metal and Brønsted acid catalyst under mild conditions[8–10] to deconstruct POs into valuable petrochemical products like naphtha (C_5–C_{12}), a primary feedstock for ethylene, propylene, and plastics production. Prior PO hydrocracking work has predominantly used noble metals (Pt, Pd, and Ru) supported on acidic supports (WO_3/ZrO_2, HY, Beta, and ZSM-5).[11–17] Although noble metal-based catalysts are active at milder temperatures, their scarcity and cost limit their industrial applications. Developing efficient Earth-abundant metal (EAM) catalyst alternatives is essential.

Bifunctional nickel-based catalysts are appealing EAM alternatives. Previous work utilizing Ni/ZSM-5, Ni/TiO_2-A-SG, and Ni/WO_x-ZrO_2 demonstrated comparable hydrocracking performance to noble metal-based catalysts.[11,18,19] However,

[a]*Department of Chemical and Biomolecular Engineering, University of Delaware, 150 Academy St, Newark, DE 19716, USA. E-mail: vlachos@udel.edu*
[b]*Center for Plastics Innovation, University of Delaware, 221 Academy St, Newark, DE 19716, USA*
[c]*Delaware Energy Institute, University of Delaware, 221 Academy St, Newark, DE, 19716, USA*

†Electronic supplementary information (ESI) available: Additional experimental details regarding catalyst reactivity, reusability, and characterization. See DOI: https://doi.org/10.1039/d5gc00345h

these catalysts exhibit notably lower naphtha selectivity and often utilize high catalyst/polymer ratios as well as elevated reaction temperatures and pressures.[11,18,19] Our group previously demonstrated that nickel supported on BEA zeolite (Ni/BEA) effectively and selectively converts LDPE to naphtha. However, the catalyst is susceptible to coking, which can be mitigated by operating at higher reaction pressures (60 bar).[20] Ceria (CeO_2) is an inexpensive structural and electronic promoter extensively used in heterogeneous catalysis.[21,22] Specifically, doping catalysts with CeO_2 can significantly alter metal dispersion, surface acidity, and overall redox behavior.[23–28] Recent studies from multiple groups have reported enhanced PO hydrocracking activity using CeO_2-promoted Pt/HY catalysts.[13,14] These initial insights motivate further exploration of Earth-abundant Ni-based catalysts, particularly the promotional role of ceria and the ceria–metal synergy in PO hydrocracking chemistry, which remain elusive.

Herein, we focus on improving the efficiency and stability of the previously reported Ni/BEA[20] catalyst by ceria incorporation. We show the promotional effect of CeO_2 doping in enhancing Ni/BEA catalytic activity and stability and demonstrate its superior naphtha selectivity. The impact of Ni–Ce electronic synergy on overall catalyst reducibility, acidity, and morphology is evaluated. Finally, we reveal the critical influence of CeO_2 on reaction pressure requirements, metal hydrogenation ability, and enhancing hydrogen storage capacity in polyolefin hydrocracking.

Materials and methods

Catalyst preparation

Nickel on beta zeolite (Ni/BEA) was synthesized using wetness impregnation. Beta zeolite support, BEA(25) (Zeolyst, Zeolite Ammonium Beta Powder, CP814E, Si/Al = 25), was first calcined at 550 °C for 4 h (2 °C min^{-1} ramp rate) to obtain the H^+ form. The zeolite was then impregnated dropwise with an appropriate amount of nickel(II) nitrate hexahydrate (Sigma-Aldrich, $Ni(NO_3)_2{\cdot}6H_2O$, 99.999% trace metal) in a DI water solution to achieve 5% Ni loading (5Ni/BEA). Nickel–ceria on BEA zeolite (5Ni%Ce/BEA) was synthesized *via* co-impregnation using $Ni(NO_3)_2{\cdot}6H_2O$ and cerium(III) nitrate hexahydrate (Sigma-Aldrich, $Ce(NO_3)_3{\cdot}6H_2O$, 99.999% trace metal). A nominal 5% Ni loading was used for all catalysts, with various %Ce metal loadings. Hereafter, the number preceding Ce indicates the weight percent of the added Ce (*e.g.*, 20Ce). For physical mixture experiments, commercial CeO_2 (Alfa Aesar by Thermo Scientific, cerium(IV) oxide, 99.5% REO) was purchased and calcined at 550 °C for 4 h in air. $5Ni/CeO_2$ was synthesized using wetness impregnation.

For wetness impregnation synthesis, all catalyst suspensions were continuously stirred using a glass rod on a hot plate set to 70 °C, then dried in air at 110 °C overnight, and calcined in air at 550 °C for 4 h (2 °C min^{-1} ramp rate). Prior to the reaction, all catalysts were reduced in a 50 : 50 (vol%) flow of H_2 and He at 350 °C for 2 h with a 10 °C min^{-1} ramping rate.

Catalyst characterization

Transmission electron microscopy. Particle size distributions were obtained with high-resolution transmission electron microscopy (HRTEM) using a field emission gun transmission electron microscope (JEOL, JEM2010F) with an accelerating voltage of 200 kV. Catalysts were dispersed in acetone and deposited on copper grids containing lacey carbon (Ted Pella, Inc. cat. #01881). The Gatan Digital Micrograph and ImageJ software were used for analysis.

Scanning electron microscopy. Metal loading was verified using scanning electron microscopy (SEM) coupled with energy-dispersive X-ray spectroscopy (EDX). Analysis was performed on an Auriga 60 microscope (Carl Zeiss NTS GmbH, Germany) equipped with a Schottky field emission gun.

N_2 physisorption. The BET surface area and porosity were measured using N_2 sorption isotherms at −196 °C on a Micromeritics ASAP 2020 instrument. The catalysts were degassed at 200 °C for 12 h under a 1 Pa vacuum prior to measurements.

X-ray fluorescence spectroscopy. X-ray fluorescence spectroscopy (XRF) measurements were obtained using a Rigaku Supermini 200 WDXRF in a He atmosphere.

X-ray diffraction. X-ray diffraction (XRD) patterns were obtained using a Bruker D8 diffractometer with a 0.05° 2θ step size, ranging from 5 to 90°, using a Cu K_α source.

Air-free X-ray photoelectron spectroscopy. X-ray photoelectron spectroscopy (XPS) was performed using a Thermo Fisher K-Alpha+ machine with an Al-Kα monochromatic source. Catalyst powders were pre-reduced in a tubular flow reactor using a 50 : 50 (vol%) mixture of H_2 and He at 350 °C for 2 h (10 °C min^{-1} ramping rate) and then transferred to an N_2 environment glove box (P_{O_2} < 500 ppm). Furthermore, the samples were pressed onto carbon tape and placed in a transfer vacuum vessel for XPS measurements without air exposure. All data processing was conducted using the Casa XPS software.

Thermogravimetric analysis. Thermogravimetric analysis (TGA) was conducted using a TA Instruments Q600. Approximately 5 mg of catalyst was placed in an alumina pan and heated from 35 °C to 700 °C (10 °C min^{-1}) under an airflow of 50 cm^3 min^{-1}.

H_2-temperature programmed reduction. H_2-temperature programmed reduction (H_2-TPR) was performed using a Micromeritics AutoChem II 2920 instrument. Approximately 0.1 g of sample was packed in a U-shaped quartz reactor, pretreated under an Ar flow (50 mL min^{-1}) at 300 °C with 2 h dwell time, and then cooled to room temperature. Once cooled, the samples were purged isothermally for 1 h in pure Ar and then heated to 900 °C at a ramp rate of 10 °C min^{-1}, with an online thermal conductivity detector (TCD) recording hydrogen consumption.

CO chemisorption. CO chemisorption pulse measurements were conducted using a Micromeritics AutoChem II 2920

instrument. A 0.05–0.1 g sample was used for each measurement. Prior to pulse measurements, the catalysts were reduced *in situ* at 350 °C under 10% H_2/Ar atmosphere at a ramp rate of 10 °C min^{-1} for 2 h, then purged in pure Ar flow for 1 h at 350 °C. The sample was then cooled to 35 °C under an Ar flow for 60 min, and a 10% CO/Ar mixture was used to saturate the catalyst over the course of 15 pulses, with a 5 min waiting time between consecutive pulses. The catalyst dispersion was calculated as $D_{Ni} = \frac{n_{CO}}{3 \times (x_{Ni}/M_{wNi})} \times 100\%$ using a molar stoichiometry factor of Ni/CO equal to 1 : 3.[29] Here, n_{CO} represents the moles of CO uptake per mass of catalyst, x_{Ni} is the Ni loading (wt%) and M_{wNi} is the molecular weight of Ni.

H_2 pulse chemisorption. H_2 pulse chemisorption measurements were performed using a Micromeritics AutoChem II 2920 instrument in pulse mode. Approximately 0.06 g of sample was packed in a U-shaped quartz reactor for each measurement. Prior to H_2 adsorption, the sample was pretreated *in situ* under a 10% H_2/Ar flow for 2 h at 350 °C and then purged in pure Ar flow for 1 h at 350 °C. The sample was cooled under Ar flow to −76 °C using a liquid N_2-ethanol slurry and treated in a 1% O_2/He mixture for 15 min at −76 °C to allow surface oxidation. After oxidation treatment, the catalyst was purged in Ar flow for 15 min. The catalyst was then heated in Ar flow to 100 °C, maintained for 1 h, and finally subjected to H_2 pulse chemisorption at 100 °C using 10 consecutive pulses with a 5 min waiting time between pulses.

FTIR pyridine thermodesorption. Fourier transform infrared (FTIR) spectra of adsorbed pyridine followed by pyridine thermodesorption were recorded in transmission mode in a Pyrex tubular flow cell equipped with 32 mm KBr windows. The pre-reduced catalyst was pressed into a self-supported wafer (~0.015 g, 1.3 cm^2, and 40 bar cm^{-2} pressure), then placed in a quartz sample holder, and pretreated in a 50 : 50 vol% H_2 : Ar flow at 300 °C (ramping rate 10 °C min^{-1}) for 2 h. After reduction, the gas flow was switched to pure Ar, the temperature was reduced to 150 °C, and a pre-pyridine saturation spectrum was recorded. Then, 5 μl of liquid pyridine (Sigma-Aldrich, 99.8%) was injected through a septum port using a micro syringe, and the pyridine vapor was allowed to saturate the sample for 30 min. The spectrum of the pyridine-saturated sample was then recorded, and the temperature was increased stepwise from 150 °C to 300 °C in a constant flow of Ar. Finally, spectra were recorded every 15 °C, and peak integration at 1540 cm^{-1} for pyridinium ions (PyH^+) bonded to Brønsted sites and 1450 cm^{-1} for Py coordinately bonded to Lewis sites (PyL) was performed using the OMNIC 8.2 software. Molar extinction coefficients reported by Tamura *et al.* were used to calculate acid site densities.[30]

FTIR H–D exchange thermodesorption. FTIR spectra of H–D exchange followed by thermodesorption were recorded in transmission mode using the same Pyrex tubular flow cell setup as in the FTIR pyridine thermodesorption experiments. Pre-reduced catalysts were pressed into a self-supported wafer and pretreated in a 50 : 50 vol% H_2 : Ar flow at 300 °C (ramping rate 10 °C min^{-1}) for 2 h. After reduction, the gas flow was switched to pure Ar, and the temperature was reduced to 50 °C under Ar flow. The cell was then purged with D_2 flow (30 mL min^{-1}) for 0.5 h. After saturation, the temperature was increased stepwise from 150 °C to 230 °C under a constant flow of D_2. Finally, spectra were recorded every 15 °C and analyzed using the OMNIC 8.2 software.

Reactivity tests

Hydrocracking experiments. 0.025 g of freshly reduced catalyst and 2.0 g of low-density polyethylene plastic feedstock (LDPE, Sigma-Aldrich, $M_w \sim 76$ kDa) were mechanically combined inside a 50 mL stainless-steel Parr batch reactor with a stir bar (25.4 mm × 8 mm, PTFE). The reactor was sealed and purged 5 times with H_2 and then charged to a final reaction pressure of 30 bar (at 20 °C). The reactor was heated to 300 °C using a band heater and hot plate, and stirring (500 rpm) was initiated once the reactor temperature reached 120 °C (LDPE melting point). The reaction was maintained at 300 °C for specified intervals, and the reactor was quenched in a water-ice bath to temperatures below 5 °C to stop the reaction. Once the reactor was cooled below 5 °C, solid, liquid, and gaseous products were collected.

Physical mixture experiments. LDPE hydrocracking reactions were also conducted using physical mixtures of BEA, 5Ni/BEA, 5Ni/CeO_2, 5Ni20Ce/BEA, and CeO_2. Binary mixtures of the catalysts were used in these experiments. Each reaction was conducted at 300 °C for 1 h under 30 bar H_2 using 2 g of LDPE. The total catalyst amount was adjusted to maintain equal metal wt% of Ni and Ce, 5% and 20%, respectively, across all mixture experiments. The same reaction procedure (as stated above), product collection and quantification method were followed.

Hydrogenation probe reactions. Hydrogenation experiments of naphthalene ($C_{10}H_8$, Sigma Aldrich, $M_w \sim 128.17$ g mol^{-1}) were conducted using 0.025 g of freshly reduced catalyst and 1.0 g of naphthalene powder. The catalyst and reactant were combined inside the same Parr batch reactor and charged to 30 bar. The reaction was conducted at 300 °C using a band heater and hot plate, and stirring (500 rpm) was initiated once the reactor temperature reached 80 °C (naphthalene melting point). The reaction was maintained for short reaction times (1 h) to avoid extensive hydrocracking side reactions and quenched in a water bath to room temperature (20 °C) for product collection.

Product analysis. The gaseous products (C_1–C_6 range) from the Parr reactor headspace were collected in a 1 L Tedlar bag at temperatures below 5 °C and analyzed using gas chromatography (GC)-FID (Agilent CP Volamine) with standard calibration mixtures (Fig. S16†). Liquid (C_4–C_{35}) and solid products (non-soluble) were collected from the reactor and extracted with ~20 mL dichloromethane (CH_2Cl_2, Fisher Chemical, ≥99.9%) containing 0.02 g of *n*-octacosane (TCI America) as an internal standard. The extracted liquid mixture was then filtered (Whatman filter paper, 100 μm) into a 100 mL round bottom flask. The liquids (C_4–C_{35}) were quantified using a GC-FID (Agilent HP-1 column) and identified using GC-mass spectrometry (MS) (Agilent DB-1 column).

Calibration coefficients and retention times for gas and liquid products were measured by injection of C_1–C_{35} analytical standards (Fig. S17†). The gas fraction was obtained using standard calibration mixtures, and the liquid products were calculated using GC-FID *via* calibration curves; the mass of the residual solid product fraction was obtained gravimetrically.

Product yields and selectivity to the liquid, solid, and gas products were calculated on a molar carbon basis. Quantification was performed using the following equations:

$$\text{LDPE conversion \%} = \frac{m_{\text{iLDPE}} - m_{\text{fLDPE}}}{m_{\text{iLDPE}}} \times 100\%$$

$$\text{Product yield}: Y_i = \frac{n_i}{n_{\text{initial}}} \times 100\%$$

$$\text{Selectivity \%} = \frac{Y_i}{\text{Total extractable products molar carbon yield}} \times 100\%$$

where m_{iLDPE} and m_{fLDPE} represent the mass of the initial LDPE polymer and final solid residue, respectively. n_i represents the moles of carbon in the product group with i carbons, and n_{initial} represents the moles of carbon in the initial polymer.

Collection and quantification of gas products extracted from naphthalene hydrogenation probe reactions followed the same procedure. The liquid products were extracted using 0.02 g of *n*-octacosane as an internal standard and quantified using the same GC-FID and GC-MS methods. Calibration coefficients and retention times for the major liquid products were measured by injecting naphthalene, tetralin (1,2,3,4-tetrahydronaphthalene, Sigma Aldrich), and *cis*/*trans*-decalin (decahydronaphthalene, Sigma Aldrich) as standards. Naphthalene conversion, tetralin yield, and selectivity were calculated from the liquid molar quantities measured using GC-FID calibration curves (Fig. S14 and S15†), and the mass of the residual naphthalene solid was obtained gravimetrically.

Results and discussion

Promotional effect of ceria on LDPE hydrocracking

The catalytic performance of 5Ni/BEA (5% Ni by weight) and Ce-promoted 5Ni%Ce/BEA (%Ce = 5, 10, 20, 30, 40 by weight) catalysts for LDPE hydrocracking at 300 °C is shown in Fig. 1. The hydrocracking activity follows a volcano-like trend with increasing Ce incorporation (Fig. 1a). After 1 h reaction time, 5Ni20Ce/BEA (20Ce) exhibited a maximum 72% yield of extractable products (C_1–C_{20}), and the LDPE conversion increased from 63% over 5Ni/BEA (5Ni) to 86% over 20Ce. Excess Ce loadings (Ce > 20%) resulted in high solid yields and decreased LDPE conversion (Fig. 1a). N_2 physisorption measurements (Table 1) indicate reduced surface area and micropore volume when excess Ce loadings (Ce > 20%) were used, suggesting physical pore blockage and coverage of the Ni and Brønsted acid sites responsible for C–C scission.

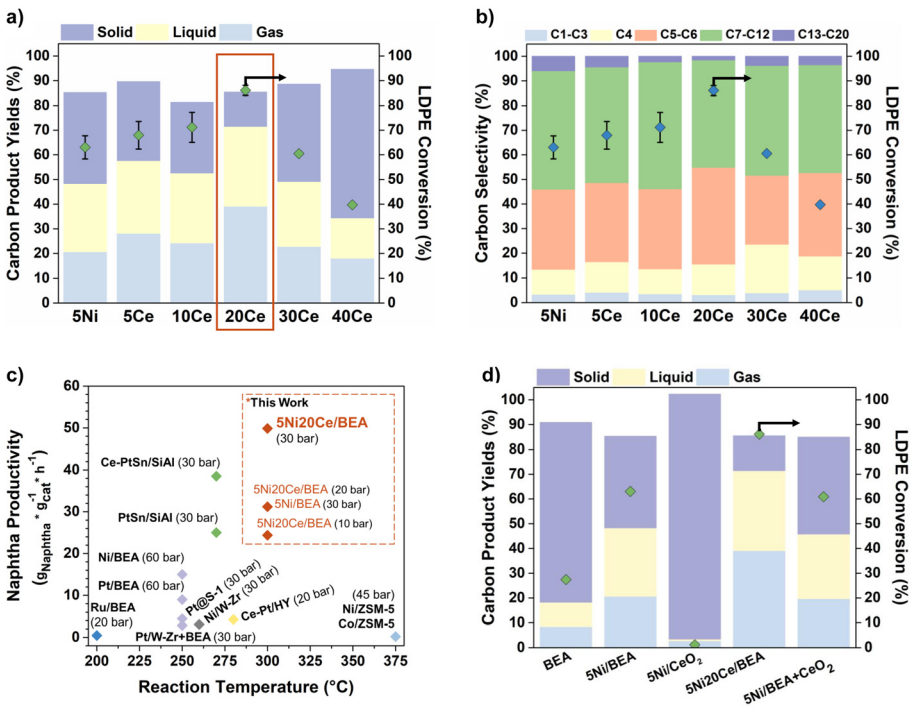

Fig. 1 (a) Hydrocracking carbon product yields (solid, liquid, and gas) and conversion for 2 g LDPE using 0.025 g 5Ni%Ce/BEA (% = 0, 5, 10, 20, 30, 40) at 300 °C, 30 bar H_2 for 1 h. Error bars represent the conversion standard deviation for 3 repeated experiments. (b) LDPE hydrocracking product selectivity distributions. (c) Naphtha productivity of this work and literature catalysts (Table S1†).[11–16,18,20] (d) Physical mixture experiments with total wt% of Ni and Ce at 5% and 20%, respectively, under the same conditions.

Table 1 Summary of catalyst characterization

Cat.	TEM d_p [a] (nm)	CO uptake[b] (μmol g^{-1})	D_{Ni} [b] (%)	BAS[c] (μmol g^{-1})	LAS[c] (μmol g^{-1})	BET surface area (m^2 g^{-1})	External surface area[d] (m^2 g^{-1})	V_{micro} [d] (cm^3 g^{-1})
BEA	—	—	—	317	230	432	207	0.21
5Ni	9.9 ± 6.6	75	2.9	50	132	432	250	0.17
5Ce	4.5 ± 2.0	109	4.3	78	158	401	229	0.16
10Ce	3.7 ± 1.6	104	4.1	68	182	358	201	0.15
20Ce	3.6 ± 1.2	105	4.1	91	278	303	163	0.13
30Ce	—	76	3.0	—	—	230	132	0.09
40Ce	—	60	2.3	—	—	171	100	0.09

[a] Particle diameter (d_p) measured from TEM distributions (Fig. 2 and S3†). [b] Ni dispersion (D_{Ni}) measured from CO chemisorption. [c] Measured from FTIR pyridine adsorption. [d] Obtained from BET *t*-plot results.

The incorporation of ceria does not significantly impact the extractable (C_1–C_{20}) product distribution (Fig. 1b, and S1a†); the overall selectivity to liquid products (>C_4) remains constant (~90%). Previous work showed that 5Ni/BEA is highly selective to naphtha (C_5–C_{12}) at 60 bar H_2 and 250 °C.[20] The 20Ce-promoted catalyst achieves a comparable 80% naphtha selectivity at a lower 30 bar H_2 pressure and 300 °C. The naphtha productivity, calculated as $g_{naphtha}\ g_{cat}^{-1}\ h^{-1}$, underscores that 20Ce outperforms other hydrocracking catalysts (Fig. 1c, and Table S1†) reported thus far. Operating at 300 °C and 30 bar H_2, the 20Ce catalyst exhibits a productivity of 50 $g_{naphtha}\ g_{cat}^{-1}\ h^{-1}$, which greatly exceeds other EAM catalysts (Ni/BEA, Ni/ZSM-5, Co/ZSM-5, and Ni-WO_x-ZrO_2) reported in the literature.[11,18,20] Furthermore, even under reduced H_2 pressures (P_{H_2} < 30 bar), the 20Ce catalyst maintains high activity comparable to that of conventional Pt-based catalysts (Fig. 1c). While noble-metal catalysts may operate at slightly lower temperatures (250–280 °C), the 20Ce catalyst achieves the highest naphtha productivity overall, highlighting its potential as an attractive EAM option for industrial applications.

To obtain insights into the promotional effect of Ce on hydrocracking activity (Fig. 1a, selectivity shown in Fig. S1b†), a physical catalyst mixture of 5Ni/BEA and CeO_2 was also investigated (Fig. 1d). The LDPE conversion of 61% was significantly lower than the 86% achieved by 20Ce but comparable to the 63% observed for 5Ni, suggesting that physically adding CeO_2 does not impact reactivity. 5Ni/CeO_2 was inactive for hydrocracking (<5% LDPE conversion) due to the lack of acid sites, indicating that the 20Ce's improved activity does not stem from Ni/CeO_2 particles (Fig. 1d). These results indicate a synergy between Ni and ceria in the 20Ce catalyst that cannot be replicated with a physical mixture.

Structural and electronic impact of Ce doping

The volcano trend in Fig. 1a suggests that an optimal fraction of Ce doping creates synergy with Ni by altering the structural and electronic properties of the catalyst. We first turn to catalyst structural characterization. HRTEM (Fig. 2a & d, Table 1) shows that Ce incorporation reduced the average Ni particle size by ~2.5×, from an average nanoparticle diameter of d_{Ni} ~ 9.9 nm (5Ni) to 3.6 nm (20Ce). The 5Ni catalyst has a broader distribution of particle sizes (Fig. 2a–c), exhibiting much larger particles d_{Ni} ~ 20 nm and aggregates (d_{Ni} > 20 nm, Fig. S2a–c†). TEM *d*-lattice spacing (d_s) measurements[31,32] of the 20Ce-promoted catalyst confirmed its compositional heterogeneity, revealing a mixture of Ni nanoparticles on the BEA support (Fig. 2e and S2d†) and Ni particles near CeO_2 (Fig. 2f and S2e†). Overall, the 20Ce catalyst exhibited a narrower particle size distribution (Fig. 2d), indicating that ceria prevents Ni agglomeration and improves particle size uniformity (Fig. S2f†). Increased CO uptake from CO chemisorption results (Table 1) further verified that ceria significantly improves Ni metal dispersion.

The Ce promotional effect on metal dispersion and sintering resistance is consistent with prior works.[13,14] Metal particle size often plays a vital role in modulating catalytic activity in structure-sensitive reactions, including hydrogen-assisted reactions like PO hydrogenolysis.[33–35] However, metal particle size does not significantly affect PO hydrocracking, as cracking is often limited by the strength and density of the zeolite's Brønsted acid sites (BAS) instead.[10] Given that the mean Ni particle size and metal dispersion (Table 1, and Fig. S3†) do not change significantly between 5% and 20% Ce loadings, the increased activity shown in Fig. 1a does not strongly correlate with the Ni particle size and dispersion.

The Ni and Ce loadings in each catalyst, verified by XRF (Table S2†) and SEM-EDX elemental mapping (Fig. S4†), were close to the theoretical loadings. Additionally, the formation of segregated bulk CeO_2 was not observed (Fig. S4†). BET surface area and pore volume measurements using N_2 physisorption are shown in Table 1. A decrease in external surface area and micropore volume is observed as the Ce loading is increased, indicating the presence of CeO_2 on both internal and external pore sites. In Fig. S5,† XRD patterns of Ce-promoted catalysts exhibit a noticeable peak at 2Θ = 28.5° corresponding to the CeO_2(111) crystal facet.[32,36] As the Ce loading increases from 5% to 20%, other prominent diffraction peaks characteristic of the face-centered cubic (fcc) CeO_2 fluorite structure [*i.e.*, 2Θ = 33.2° (200), 47.4° (220) and 56.4° (222)] become visible, suggesting the growth of CeO_2 particles.[32,36] Additionally, the relative peak intensities corresponding to metallic Ni [2Θ = 44.5°(111), 52.1°(200)] and NiO [2Θ = 37.2°(111), 43.5°(200)] decrease significantly.[37] Diffraction peaks associated with Ni/NiO are no longer visible in the 20Ce-promoted catalyst, indi-

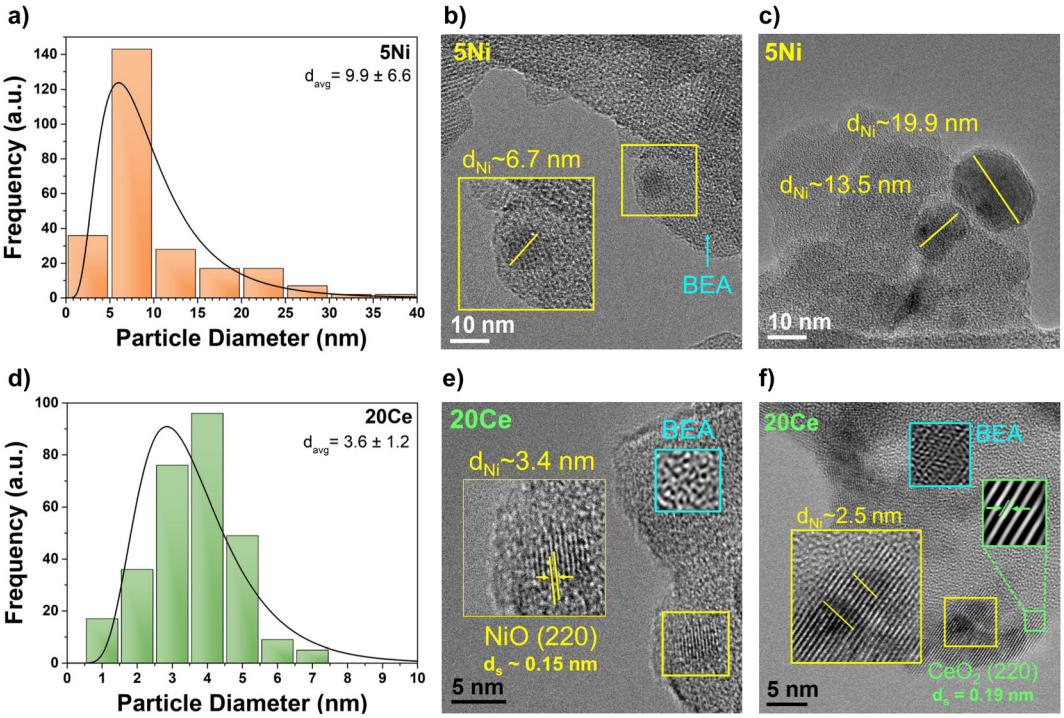

Fig. 2 Particle size distributions and HRTEM micrographs of (a–c) 5Ni/BEA (5Ni) and (d–f) 5Ni20Ce/BEA (20Ce).

cating a small Ni crystallite size below the detection limit of XRD and a higher Ni dispersion, consistent with HRTEM (Fig. 2) and CO chemisorption (Table 1) results.

Acid site characterization *via* pyridine FTIR (Table 1 and Fig. S6†) revealed that the parent BEA zeolite contains high BAS and Lewis acid site (LAS) densities. As expected, the deposition of Ni on the zeolite support significantly reduced both BAS and LAS densities due to acid site coverage. 5Ni exhibited a LAS density of ~132 μmol g_{cat}^{-1} and a BAS density of ~50 μmol g_{cat}^{-1}. Due to the strong Lewis acidity of cerium cations, Ce addition drastically increased the LAS density (Table 1).[38] At 20Ce loading, the LAS density increased to ~278 μmol g_{cat}^{-1} and the BAS density to ~91 μmol g_{cat}^{-1}. Increasing Ce loading increases the LAS density but only marginally affects the BAS density. CeO_2 is a reducible oxide primarily possessing LAS. Due to oxygen vacancies in the CeO_2 crystal lattice, surface hydroxyls can form on Ce^{3+} sites and create Brønsted acidity, rationalizing the slight increase in BAS.[38,39] Yet, we hypothesize that these additional sites do not significantly impact the overall cracking rate since the stronger Brønsted acid sites of the zeolite are responsible for skeletal rearrangement and beta scission.

To understand the redox and electronic properties imparted by Ce incorporation, the catalysts were characterized using TPR and XPS (Fig. 3). TPR profiles for the 5Ni and Ce-promoted Ni catalysts are shown in Fig. 3a. The reduction of 5Ni exhibited a broad peak with multiple local maxima, indicating a heterogeneous mixture of Ni species (Fig. 3a) with a broad particle size distribution. The lower temperature maximum at ~340 °C has been ascribed to the direct reduction of bulk NiO species located on the external pore sites of the zeolite.[23,24] Although the exact attribution of the peaks is difficult to ascertain, the higher temperature peaks at ~392 °C and 425 °C are associated with the reduction of dispersed NiO species confined within the internal pores and interacting strongly with the support.[24,26,28] Upon adding Ce, the main reduction peak becomes unimodal, with different NiO species becoming indistinguishable, reflecting a narrower particle size distribution consistent with the TEM analysis (Fig. 2). Furthermore, the main Ni reduction peak gradually shifts to lower temperatures and includes the partial reduction of Ce^{4+} to Ce^{3+}. Higher temperature peaks (>400 °C), corresponding to the surface and bulk reduction of pure CeO_2, were not observed for Ce-promoted Ni catalysts (Fig. 3a), demonstrating that the strong redox interaction between Ni and CeO_2 promotes the co-reduction of both species under milder conditions.

XPS spectra of the Ni $3p_{3/2}$ region for the reduced (350 °C) catalysts are shown in Fig. 3b. The 5Ni catalyst exhibits a prominent Ni $3p_{3/2}$ peak centered at a binding energy (BE) of 853.7 eV assigned to NiO (Ni^{2+}) and a second peak at 858.6 eV corresponding to the broad satellite.[40–42] With the incorporation of 5–10% Ce, the Ni $3p_{3/2}$ peak remains centered around 853.7 eV but begins to broaden, implying a more complex electronic environment of Ni oxidation states (Fig. 3b and Table S3†). Upon 20Ce addition, a broad feature at 855.2 eV associated with $Ni(OH)_2$ species (ascribed to BE ~ 856.2 eV)[40–42] becomes more apparent, likely due to the partial reduction of NiO, implying the presence of $Ni^{\delta+}$ species.

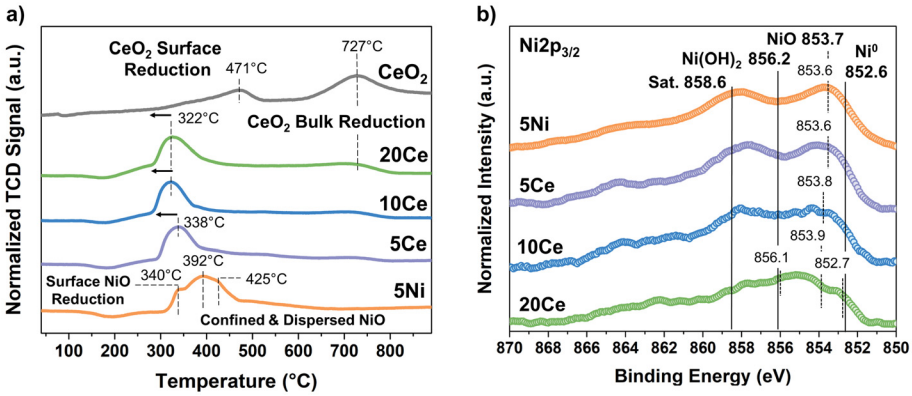

Fig. 3 Characterization of 5Ni%Ce/BEA (%Ce = 0, 5, 10, 20) catalysts: 5Ni (orange), 5Ce (purple), 10Ce (blue), and 20Ce (green). (a) H_2-TPR profiles. (b) Air-free XPS spectra of the Ni $3p_{3/2}$ region normalized to C 1s at 284.8 eV.

Furthermore, the Ni $3p_{3/2}$ peak shifts to a lower BE around 852.7 eV, close to the Ni^0 state at 852.6 eV,[40–42] indicating contributions from metallic Ni species. The presence of ceria facilitates the reduction of Ni^{2+} species, as higher fractions of Ni^0 (Table S3†) are observed, which further corroborates the improved Ni reducibility observed in TPR (Fig. 3a). Additionally, XPS spectra of the Ce 3d region (Fig. S7†) reveal the co-existence of both Ce^{4+} and Ce^{3+} electronic states, indicating the co-reduction of Ni and Ce species (Fig. 3a) at lower temperatures. Clearly, the electronic synergy of Ni and Ce species alters the overall redox properties and enhances the *in situ* catalyst reduction under reaction conditions.

To investigate the stability of the Ce-promoted catalysts, the coke content on spent catalysts was analyzed using TGA under an air atmosphere. Spent catalysts were collected after a 3.5 h reaction to ensure maximum conversion (Fig. S8†). Fig. 4a shows that the quantity of coke decreased with increasing Ce loading. The 20Ce-promoted catalyst exhibited 6% less total mass loss compared to 5Ni. Furthermore, the composition of the coke was also affected (Fig. 4a); the ratio of light coke (mass loss 100–350 °C) to heavy polyaromatic coke (mass loss >350 °C) is shown in Fig. 4b. Light coke has been attributed to lighter organic residues that can easily be removed under reaction conditions (300 °C, 30 bar H_2). Meanwhile, heavy coke deposits form by olefin intermediate oligomerization during hydrocracking, blocking pore openings and active sites, which hinder catalytic activity. Upon adding Ce, an overall reduction in coke is observed (Fig. 4b). We rationalize that the reduction in coke, specifically heavy coke, on the Ce-promoted Ni catalysts implies that ceria promotes the hydrogenation and desorption of adsorbed intermediates (coke precursors).

Direct reuse of the spent 5Ni and 20Ce catalysts in 3 successive reaction cycles revealed significant deactivation (Fig. S9a & b†) and coking, but 20Ce still exhibited higher resistance to coking (Fig. S10a & b†). Ceria likely promotes the desorption of adsorbed species on the Ni site but coking of the Brønsted acid sites, as well as the oligomerization and migration of heavy coke during the reduction process, may contribute to additional deactivation and overall loss of activity after 3 uses. Both catalysts were fully regenerable (*via* calcination and reduction) and demonstrated comparable activity and naphtha selectivity to the fresh catalysts (Fig. S9c & d and S10c & d†). Additional details can be found in the ESI, Fig. S9–S11.†

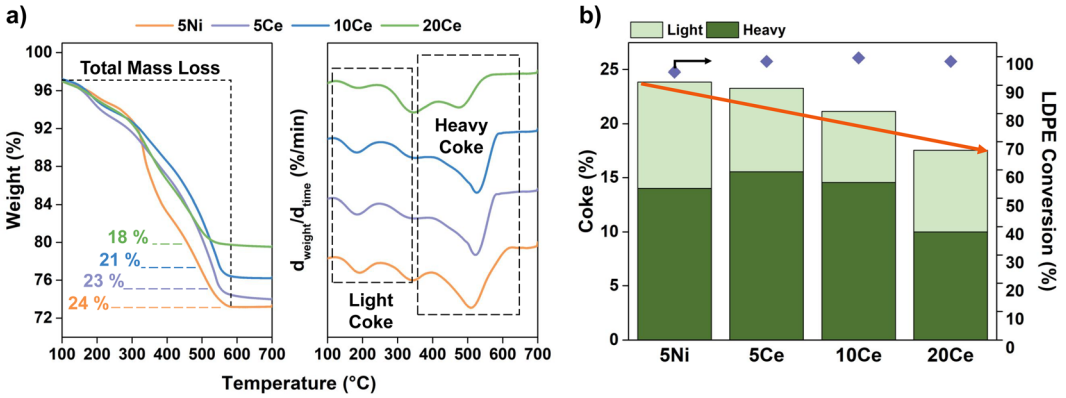

Fig. 4 TGA thermograms of (a) weight loss (%) and derivative weight loss (% min^{-1}) and (b) light/heavy coke content comparison for the spent 5Ni/BEA (5Ni) and Ce-promoted 5Ni%Ce/BEA (%Ce = 0, 5, 10, 20) catalysts after 3.5 h hydrocracking reaction (2 g LDPE, 0.025 g catalyst, 300 °C, 30 bar).

Role of H_2 and hydrogenation rates

It was previously demonstrated that over 5Ni/BEA, higher hydrogen pressures (P_{H_2}) of 60 bar were necessary to limit catalyst coking and achieve adequate LDPE deconstruction and high naphtha yields.[20] P_{H_2} variation strongly affects PO hydrocracking and correlates strongly with the Ni hydrogenation ability, a critical step in the overall mechanism.[20] As such, the hydrocracking of LDPE was conducted under varying P_{H_2} for the 5Ni and 20Ce catalysts, as shown in Fig. 5a. As the P_{H_2} decreased from 30 to 10 bar, the LDPE conversion over 5Ni decreased from 60 to 45% (Fig. 5a, selectivity in Fig. S12a†). In this pressure range, the liquid products had a yellow hue, indicative of olefinic, aromatic, and cyclic alkane precursors to coke (Fig. 5a and S13†). The liquid products remained clear for $P_{H_2} \geq 30$ bar, implying less coke precursors. Without ceria, the 5Ni activity increases significantly (from 60% to 88% LDPE conversion) when P_{H_2} increases from 30 to 40 bar. This suggests that the excess hydrogen saturates the Ni surface, stimulating the hydrogenation of adsorbed intermediates and inhibiting coke formation even without Ce incorporation. The LDPE conversion over the 20Ce catalyst also decreased at lower pressures, confirming a positive reaction order in P_{H_2} (Fig. 5a). For $P_{H_2} \leq 20$ bar, the liquid products exhibited a yellow hue, and the LDPE conversion reduced from 85% (30 bar) to 54% (10 bar), indicating catalyst deactivation. Nonetheless, 20Ce demonstrates higher activity and naphtha selectivity (Fig. 1c and S12b†) than 5Ni, even under hydrogen-deficient conditions ($P_{H_2} < 30$ bar).

Hydrogenation of naphthalene, used as a coke surrogate for polycyclic aromatics, was conducted to probe the promotional effect of Ce on Ni hydrogenation ability (Fig. 5b and S14†). Fig. 5b shows that the 5Ni and 20Ce catalysts displayed similar naphthalene conversions (33% and 39%, respectively), but 20Ce exhibited 1.5× higher selectivity to the primary hydrogenated product, tetralin. The increased selectivity implies that Ce promotes naphthalene hydrogenation, corroborating our findings from TGA (Fig. 4) and pressure variation experiments (Fig. 5a). Our prior work reported that reducible oxide supports, including CeO_2, can store and donate H to the metal *via* spillover, aiding unsaturated intermediates' hydrogenation during hydrogenolysis.[43,44] Likewise, we hypothesize that ceria promotes the hydrogenation of olefin intermediates and reaction products on the nearby Ni sites. This leads to their desorption, thereby prolonging catalyst performance.

Finally, *in situ* FTIR spectroscopy was used to measure H–D exchange over the 5Ni and 20Ce-promoted Ni/BEA catalysts (Fig. 5c & d). The catalysts were pre-reduced in H_2, then a con-

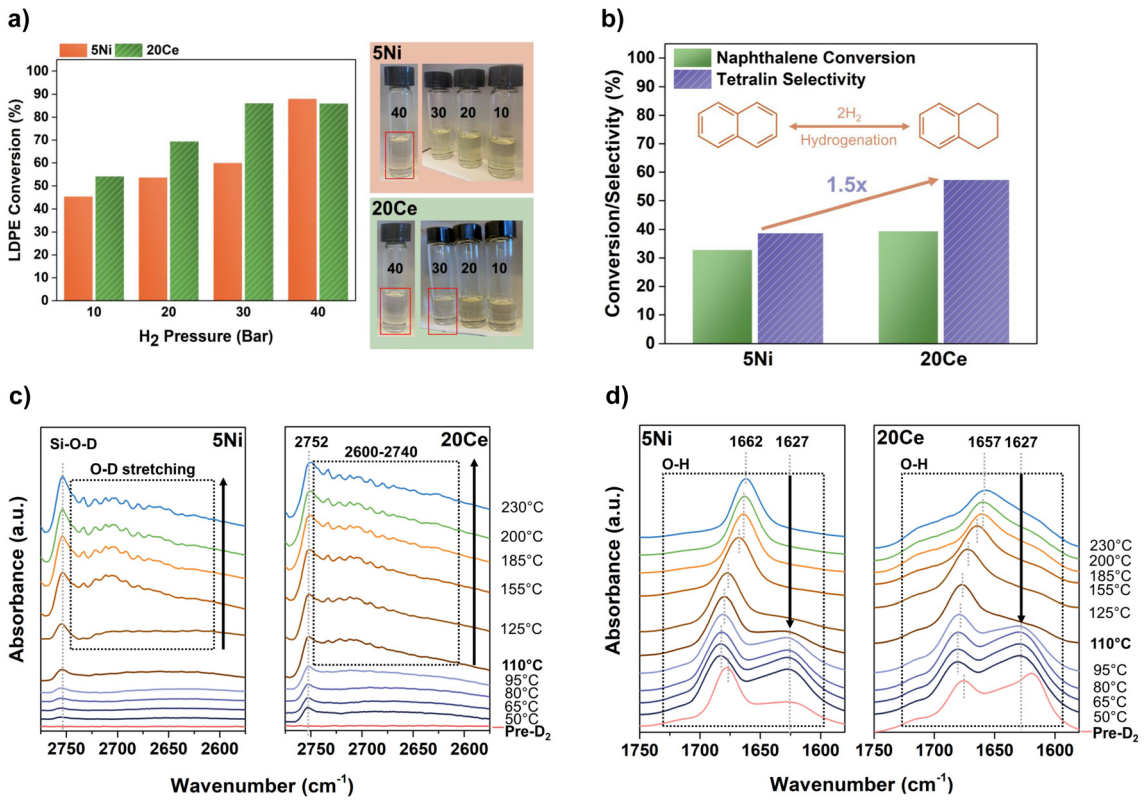

Fig. 5 (a) LDPE hydrocracking conversion and images of liquid reaction products at varying H_2 pressures for the 5Ni/BEA (5Ni) and 5Ni20Ce/BEA (20Ce) catalysts. Reaction conditions: 2 g LDPE, 0.025 g catalyst, 300 °C, 1 h. (b) Naphthalene hydrogenation reaction conversion and tetralin selectivity over the 5Ni and 20Ce catalysts. Reaction conditions: 1 g naphthalene, 0.025 g catalyst, 300 °C, 1 h. FTIR spectra of (c) O–D and (d) O–H vibrational range for H–D exchange in D_2 flow for 5Ni and 20Ce.

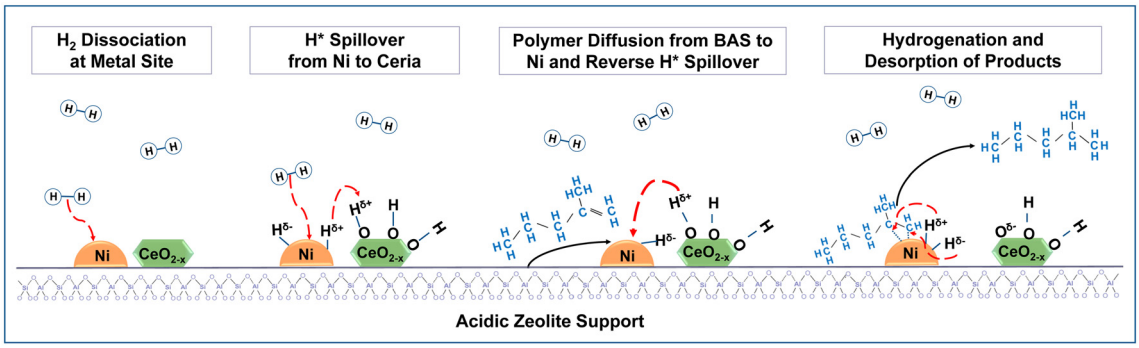

Scheme 1 Proposed role of CeO_2 in the hydrocracking reaction.

stant flow of D_2 was introduced, and the temperature was increased from 50 to 230 °C. At temperatures <100 °C, a peak at 2752 cm^{-1} appears, attributed to the H–D exchange of non-acidic silanol groups, which can undergo exchange at room temperature (Fig. 5c).[45,46] As the temperature increases, prominent O-D free stretching vibrations in the broad frequency range of 2670–2740 cm^{-1} become more pronounced, indicating the formation of different OD surface species on Ni and Ce.[47–50] During H–D exchange, a complementary decrease in the O–H vibrations in the 1600–1700 cm^{-1} range (Fig. 5d), attributed to hydrogen-bonded OH groups on the zeolite, is also observed.[49–51] For the 5Ni catalyst, H–D exchange on the non-acidic silanol groups is noticeable at <100 °C, but primary O–D stretching vibrations do not form until ≥125 °C. In contrast, over the 20Ce catalyst, the Si–O–D exchange is extremely prominent even at 50 °C, and the O–D stretching becomes apparent at temperatures as low as 95 °C and intensifies by ≥110 °C (Fig. 5c). These results imply that Ni dissociates D_2 at temperatures as low as 50 °C, and the presence of ceria increases the rate of H–D exchange, especially at lower temperatures. The faster rates of H-D exchange suggest that during PO hydrocracking, ceria may store H that spillovers from the Ni sites, thereby increasing Ni surface availability for further H_2 activation and leading to additional active H species available for hydrogenation. Lastly, H_2 chemisorption provided additional evidence supporting the role of CeO_2 as a potential hydrogen reservoir (Table S4†). The 20Ce catalyst consumed (5.14 μmol H_2 g_{cat}^{-1}) ~ 1.6× more H_2 per g_{cat} than the 5Ni catalyst (2.99 μmol H_2 g_{cat}^{-1}). This increase in H_2 adsorption further suggests that CeO_2 likely aids in the storage of activated H from Ni, which promotes additional H_2 dissociation and supports the results observed from FTIR H–D exchange.

Discussion

Recent works on Ce-promoted Pt/HY catalysts reported that Ce promotes Brønsted acidity, metal dispersion, reducibility, resistance to coking, and hydrocracking activity.[13,14] CeO_2 can alter the catalyst morphology (Fig. 2) by potentially increasing active site exposure and improving Ni dispersion. Furthermore, it can store hydrogen, a key factor in enhancing Ni reducibility and hydrogenation. Ni is a widely recognized metal whose hydrogenation ability is sensitive to H_2 availability (Fig. 5a). CeO_2 can form surface hydroxyls or hydrides (CeOH/CeH) due to the oxygen vacancies carrying excess negative charge near reduced Ce^{3+} cations.[21,52,53] The electron-rich Ce sites adjacent to oxygen vacancies store excess hydrogen as CeOH/CeH species. The formation of oxygen vacancies depends on the local degree of ceria reduction (formation of Ce^{3+} cations).[21,22,54] Under reducing conditions, ceria forms non-stochiometric CeO_{2-x} oxides ($0 < x \leq 0.5$), which contain oxygen vacancies.[21,22,54] TPR/XPS analyses show (Fig. 3 and S7†) that the synergy between Ni and CeO_2 controls the catalyst redox behavior and simultaneously reduces both species under reaction conditions. The proximity of the Ni and ceria interfaces (Fig. 2) enables active H species to readily diffuse from Ni sites to partially reduced ceria (CeO_{2-x}) *via* spillover.[21,55] CeO_{2-x} stores active H (Table S4†), increasing the availability of free sites on the Ni surface, which may promote additional H_2 dissociation (Fig. 5c & d). Ceria can donate H to Ni by reverse spillover, facilitating the hydrogenation of intermediates and reaction product desorption (Fig. 5a & b). This prevents Ni deactivation from coking (Fig. 4), enhancing hydrogenation and the apparent hydrocracking rate (Fig. 1). Scheme 1 depicts the hypothesized role of ceria in the reaction.

Conclusions

In this work, we reveal the mechanistic role of CeO_2 promoters in 5Ni/BEA catalysts for polyolefin hydrocracking. We demonstrated that 20 wt% Ce-promoted 5Ni/BEA is an effective EAM alternative to noble metal-based catalysts with superior LDPE hydrocracking activity and the highest reported naphtha productivity. Ceria stabilized smaller Ni particles (improved metal dispersion) and promoted Ni reducibility while suppressing catalyst coking and deactivation, even under H_2-deficient conditions. Probe reactions over Ce-promoted 5Ni/BEA exhibited enhanced H_2 activation/dissociation and hydrogenation ability compared to 5Ni/BEA. We hypothesize that a unique property of ceria is its ability to store hydrogen that spillovers, promoting the hydrogenation of adsorbed surface species and facili-

tating the desorption of reaction products for improved catalytic performance. The significant insights gained from this work open exciting opportunities for tuning the efficiency and stability of EAM catalysts in polyolefin waste deconstruction strategies.

Author contributions

J.A.S. and A.B. performed catalyst synthesis and reactivity tests. J.A.S. performed product and catalyst characterization and analysis. E.S. performed SEM imaging. D.G.V., J.A.S. and E.S. conceptualized the project. W.Z. and D.G.V. guided the experimental methodology and investigation. The manuscript was written by J. A. S. and revised by J.A.S., E.S. and D.G.V. with input from all authors. D.G.V. was responsible for project administration and funding acquisition.

Data availability

All data needed to evaluate the conclusions in this paper have been included in the main text or the ESI.† Additional data regarding this paper may be requested from the authors.

Conflicts of interest

The authors declare that they have no known competing financial interests or personal relationships that could have appeared to influence the work reported in this paper.

Acknowledgements

This work was supported as part of the Center for Plastics Innovation (CPI), an Energy Frontier Research Center (EFRC) supported by the U.S. Department of Energy (DOE), Office of Science, Office of Basic Energy Sciences grant number DE-SC0021166. The authors acknowledge the use of instruments in the Advanced Materials Characterization Lab (AMCL), Keck Center for Microscopy at the University of Delaware. The XPS instrumentation at the University of Delaware was supported by the National Science Foundation under grant number CHE-1428149.

References

1 O. A. Alabi, K. I. Ologbonjaye, O. Awosolu and O. E. Alalade, *J. Toxicol. Risk Assess.*, 2019, **5**, 1–13.
2 P. N. T. Pilapitiya and A. S. Ratnayake, *Cleaner Mater.*, 2024, **11**, 100220.
3 R. Geyer, in *Plastic waste and recycling*, Elsevier, Academic Press, 2020, ch. 2, pp. 13–32, DOI: 10.1016/B978-0-12-817880-5.00002-5.
4 B. Manjula, A. B. Reddy, E. R. Sadiku, V. Sivanjineyulu, G. F. Molelekwa, J. Jayaramudu and K. R. Kumar, in *Polyolefin Fibres*, Elsevier, Woodhead Publishing, 2 edn, 2017, ch. 18, pp. 539–560, DOI: 10.1016/B978-0-08-101132-4.00018-7.
5 Y. K. Kim, in *Polyolefin Fibres*, Elsevier, Woodhead Publishing, 2 edn, 2017, ch. 5, pp. 135–155, DOI: 10.1016/B978-0-08-101132-4.00005-9.
6 A. D. Patel, Z. O. Schyns, T. W. Franklin and M. P. Shaver, *Nat. Commun.*, 2024, **15**, 8733.
7 A. J. Martín, C. Mondelli, S. D. Jaydev and J. Pérez-Ramírez, *Chem*, 2021, **7**, 1487–1533.
8 J. Sun, J. Dong, L. Gao, Y.-Q. Zhao, H. Moon and S. L. Scott, *Chem. Rev.*, 2024, **124**, 9457–9579.
9 H. Wang and S. C. E. Tsang, *Cell Rep. Phys. Sci.*, 2024, **5**, 102075.
10 Z. Dong, W. Chen, K. Xu, Y. Liu, J. Wu and F. Zhang, *ACS Catal.*, 2022, **12**, 14882–14901.
11 W.-T. Lee, A. van Muyden, F. D. Bobbink, M. D. Mensi, J. R. Carullo and P. J. Dyson, *Nat. Commun.*, 2022, **13**, 4850.
12 J. E. Rorrer, A. M. Ebrahim, Y. Questell-Santiago, J. Zhu, C. Troyano-Valls, A. S. Asundi, A. E. Brenner, S. R. Bare, C. J. Tassone and G. T. Beckham, *ACS Catal.*, 2022, **12**, 13969–13979.
13 H. Wang, T. Yoskamtorn, J. Zheng, P.-L. Ho, B. Ng and S. C. E. Tsang, *ACS Catal.*, 2023, **13**, 15886–15898.
14 P. Zhao, W. Guo, Z. Gui, J. Jiang, Z. Zhu, J.-J. Li, L. Zhao, J. Zhou and Z. Xi, *ACS Sustainable Chem. Eng.*, 2024, **12**, 5738–5752.
15 S. Liu, P. A. Kots, B. C. Vance, A. Danielson and D. G. Vlachos, *Sci. Adv.*, 2021, **7**, eabf8283.
16 L. Li, H. Luo, Z. Shao, H. Zhou, J. Lu, J. Chen, C. Huang, S. Zhang, X. Liu and L. Xia, *J. Am. Chem. Soc.*, 2023, **145**, 1847–1854.
17 A. Bin Jumah, V. Anbumuthu, A. A. Tedstone and A. A. Garforth, *Ind. Eng. Chem. Res.*, 2019, **58**, 20601–20609.
18 J. Shang, Y. Li, Y. Hu, T. Zhang, T. Wang, J. Zhang, H. Yan, Y. Liu, X. Chen and X. Feng, *J. Catal.*, 2024, **430**, 115302.
19 L. Chen, J. B. Moreira, L. C. Meyer and J. Szanyi, *Appl. Catal., B*, 2023, **335**, 122897.
20 B. C. Vance, Z. Yuliu, S. Najmi, E. Selvam, J. E. Granite, K. Yu, M. G. Ierapetritou and D. G. Vlachos, *Chem. Eng. J.*, 2024, **487**, 150468.
21 A. Trovarelli, *Catal. Rev.*, 1996, **38**, 439–520.
22 M. Capdevila-Cortada, G. Vilé, D. Teschner, J. Pérez-Ramírez and N. López, *Appl. Catal., B*, 2016, **197**, 299–312.
23 D. Li, L. Zeng, X. Li, X. Wang, H. Ma, S. Assabumrungrat and J. Gong, *Appl. Catal., B*, 2015, **176**, 532–541.
24 N. Battumur, N. Sergelenbaatar, T. Bold and E. Byambajav, *J. CO2 Util.*, 2023, **68**, 102380.
25 W. Gac, W. Zawadzki, M. Greluk, G. Słowik, M. Rotko and M. Kuśmierz, *Catalysts*, 2021, **12**, 13.
26 W. Gac, W. Zawadzki, G. Słowik, W. Grudziński and S. Dzwigaj, *Catal. Today*, 2024, 114728, DOI: 10.1016/j.cattod.2024.114728.

27 W. Gac, W. Zawadzki, M. Rotko, G. Słowik and M. Greluk, *Top. Catal.*, 2019, **62**, 524–534.
28 X. Wang, L. Zhu, Y. Liu and S. Wang, *Sci. Total Environ.*, 2018, **625**, 686–695.
29 C. Bartholomew and R. Pannell, *J. Catal.*, 1980, **65**, 390–401.
30 M. Tamura, K.-i. Shimizu and A. Satsuma, *Appl. Catal., A*, 2012, **433**, 135–145.
31 C. W. Kim, Y. S. Son, A. U. Pawar, M. J. Kang, J. Y. Zheng, V. Sharma, P. Mohanty and Y. S. Kang, *J. Mater. Chem. A*, 2014, **2**, 19867–19872.
32 S. Phoka, P. Laokul, E. Swatsitang, V. Promarak, S. Seraphin and S. Maensiri, *Mater. Chem. Phys.*, 2009, **115**, 423–428.
33 L. Chen, L. C. Meyer, L. Kovarik, D. Meira, X. I. Pereira-Hernandez, H. Shi, K. Khivantsev, O. Y. Gutiérrez and J. Szanyi, *ACS Catal.*, 2022, **12**, 4618–4627.
34 M. Tamura, S. Miyaoka, Y. Nakaji, M. Tanji, S. Kumagai, Y. Nakagawa, T. Yoshioka and K. Tomishige, *Appl. Catal., B*, 2022, **318**, 121870.
35 J. A. Sun, P. A. Kots, Z. R. Hinton, N. S. Marinkovic, L. Ma, S. N. Ehrlich, W. Zheng, T. H. Epps III, L. T. Korley and D. G. Vlachos, *ACS Catal.*, 2024, **14**, 3228–3240.
36 T. S. Sreeremya, A. Krishnan, K. C. Remani, K. R. Patil, D. F. Brougham and S. Ghosh, *ACS Appl. Mater. Interfaces*, 2015, **7**, 8545–8555.
37 J. T. Richardson, R. Scates and M. V. Twigg, *Appl. Catal., A*, 2003, **246**, 137–150.
38 M. I. Zaki, M. A. Hasan, F. A. Al-Sagheer and L. Pasupulety, *Colloids Surf., A*, 2001, **190**, 261–274.
39 M. K. Gnanamani, R. Garcia, G. Jacobs, K. Góra-Marek, D. C. Cronauer, A. J. Kropf and C. L. Marshall, *Appl. Catal., A*, 2020, **602**, 117722.
40 H. Nesbitt, D. Legrand and G. Bancroft, *Phys. Chem. Miner.*, 2000, **27**, 357–366.
41 A. P. Grosvenor, M. C. Biesinger, R. S. C. Smart and N. S. McIntyre, *Surf. Sci.*, 2006, **600**, 1771–1779.
42 M. C. Biesinger, B. P. Payne, L. W. Lau, A. Gerson and R. S. C. Smart, *Surf. Interface Anal.*, 2009, **41**, 324–332.
43 C. Wang, T. Xie, P. A. Kots, B. C. Vance, K. Yu, P. Kumar, J. Fu, S. Liu, G. Tsilomelekis, E. A. Stach, W. Zheng and D. G. Vlachos, *JACS Au*, 2021, **1**, 1422–1434.
44 C. Wang, K. Yu, B. Sheludko, T. Xie, P. A. Kots, B. C. Vance, P. Kumar, E. A. Stach, W. Zheng and D. G. Vlachos, *Appl. Catal., B*, 2022, **319**, 121899.
45 R. Salzer, J. Dressler, K.-H. Steinberg, U. Roland, H. Winkler and P. Klaeboe, *Vib. Spectrosc.*, 1991, **1**, 363–369.
46 U. Roland, R. Salzer and S. Stolle, *Investigation of Hydrogen and Deuterium Spillover on Y Zeolites by FT-IR Microscopy–Rate Determining Steps*, Elsevier, 1994.
47 A. Badri, C. Binet and J.-C. Lavalley, *J. Chem. Soc., Faraday Trans.*, 1996, **92**, 4669–4673.
48 F. Gennari, T. Montini, N. Hickey, P. Fornasiero and M. Graziani, *Appl. Surf. Sci.*, 2006, **252**, 8456–8465.
49 H. Zhou, L. Chen, Y. Guo, X. Liu, X.-P. Wu, X.-Q. Gong and Y. Wang, *ACS Catal.*, 2022, **12**, 4806–4812.
50 Z. Zhao, G. Gao, Y. Xi, J. Wang, P. Sun, Q. Liu, C. Li, Z. Huang and F. Li, *Nat. Commun.*, 2024, **15**, 8444.
51 H. Yamazaki, T. Yokoi, T. Tatsumi and J. N. Kondo, *J. Phys. Chem. Lett.*, 2014, **5**, 3528–3531.
52 Z. Wu, Y. Cheng, F. Tao, L. Daemen, G. S. Foo, L. Nguyen, X. Zhang, A. Beste and A. J. Ramirez-Cuesta, *J. Am. Chem. Soc.*, 2017, **139**, 9721–9727.
53 K. Werner, X. Weng, F. Calaza, M. Sterrer, T. Kropp, J. Paier, J. Sauer, M. Wilde, K. Fukutani and S. Shaikhutdinov, *J. Am. Chem. Soc.*, 2017, **139**, 17608–17616.
54 G. Varvoutis, M. Lykaki, G. E. Marnellos and M. Konsolakis, *Catalysts*, 2023, **13**, 275.
55 W. C. J. Conner and J. L. Falconer, *Chem. Rev.*, 1995, **95**, 30.